Enhancing polycrystalline-microstructure reconstruction from X-ray diffraction microscopy with phase-field post-processing

Marcel Chlupsa^{1,†}, Zachary Croft^{2,†}, Katsuyo Thornton^{1,2,*}, Ashwin J. Shahani^{1,*}

Abstract

A novel protocol utilizing a phase-field model was used to process the reconstruction of a polycrystalline microstructure from synchrotron-based high-energy X-ray diffraction microscopy. This approach is an intuitive and standardized alternative to typical image processing routines. It preserves high-confidence regions by deploying a completeness-based mobility parameter in the phase-field model. Phase-field governing equations result in a space-filling grain map that adheres to the physics of the microstructure, *i.e.*, it penalizes high-energy grain shapes and configurations and promotes grain boundary (GB) smoothing. We quantify GB smoothing by measuring, in 2D, the circularity of interior grains and the tortuosity of individual GBs. Results are also presented in 3D. This post-processing protocol can be applied to any X-ray diffraction microscopy reconstruction that consists of a spatial map of grains and corresponding confidence values. Furthermore, it can be adapted to accommodate other types of microstructures, including those that are polyphase.

Keywords: synchrotron-based characterization, X-ray diffraction microscopy, three-dimensional microstructure, grain boundaries, phase-field simulation

¹Department of Materials Science and Engineering, University of Michigan, Ann Arbor, MI, 48109, United States

²Applied Physics Program, University of Michigan, Ann Arbor, MI, 48109, United States [†]These authors contributed equally to this work.

^{*}Corresponding authors: <u>kthorn@umich.edu</u>, <u>shahani@umich.edu</u>

Various defects arise from the arrangement of grains in a microstructure [1]. Two grains converge at a grain boundary (GB), three grains at a triple junction (TJ), and four grains at a quadruple node (QN). In 3D space, the GBs, TJs, and QNs are represented by surfaces, lines, and points, respectively. In 2D, the GBs are represented by lines and the TJs by points. Due to capillary forces and assuming a constant GB energy, a higher-order connectivity, *e.g.*, a quintuple node, is unstable in 3D (a QN is similarly unstable in 2D). The distributions of these defects can either bolster or hinder material performance depending on the specific application context. They provide pathways for crack propagation [2-4], corrosion [5, 6], and intergranular diffusion [7, 8] as a result of the weaker atomic bonding and the excess volume. Therefore, control of polycrystalline microstructure is of great importance to the manufacture of technological materials, and such control demands an understanding of the polycrystalline microstructure in all its complexity.

Peering into the 3D structure of polycrystals has proved challenging for decades [9-11] but recently the advent of laboratory- and synchrotron-based X-ray diffraction imaging has enabled researchers to uncover microstructural details nondestructively and at high spatial and temporal resolutions [12-18]. Diffraction is required because the material density is the same on either side of a GB, while the crystallographic orientation is different. Each time a grain in the bulk satisfies the Bragg condition, a diffracted beam is generated; this signal is then transmitted through the sample and collected by 2D detectors. Since different grains satisfy Braggs' law at different angles, the sample is rotated to capture all unique reflections. The microstructure of the illuminated sample volume is then reconstructed from the set of 2D diffraction images. To fully realize the utility of these modern characterization tools, we must first maximize the fidelity of the reconstructions, which are susceptible to various types and sources of errors and uncertainties inherent to the experiment. Reconstructions of polycrystalline microstructures are influenced, in practice, by heterogeneous grain size distributions, differences in scattering cross sections between phases, limited dynamic range of detectors, fluctuations in incident intensity, overlapping Bragg peaks, and other measurement errors [16]. This noise gives rise to an unphysical roughness of the GBs at the mesoscale, making it difficult to quantify GB properties, e.g., tortuosities [19-21], characters [22-24], curvatures [25], and contact affinities [26]. Uncertainties in these quantities propagate into estimations of effective diffusivity [21], corrosion resistance [6, 27], electrical resistance [28], and fracture strength [29].

In this work, we present a new post-processing protocol that utilizes a phase-field model to enhance the reconstructed microstructures by replacing the untrustworthy regions. As a proof-of-concept of our approach, we examined the shape memory alloy Cu_{71.6}Al₁₇Mn_{11.4} and thermomechanically processed it following Refs. [30] and [31]. A cylindrical 1-mm diameter sample was cut from the bulk ingot using electric discharge machining. To characterize its 3D microstructure, we conducted near-field (nf) high-energy diffraction microscopy (nf-HEDM) at the 1-ID-E beamline of Argonne National Laboratory's Advanced Photon Source (Lemont, IL, USA) [16, 32-36]. In nf-HEDM, a line-focused monochromatic X-ray beam illuminated a quasi-

2D cross-section of the sample, and diffraction images were collected at two sample-to-detector distances, 10 mm and 12 mm. For each cross-section, the sample was rotated about the vertical axis (parallel to gravity, *i.e.*, normal to the plane defined by the beam) at 0.25° intervals from 0 to 180° . Images were collected at each detector distance (yielding 1440 images for each cross-section). The first set of images was collected 3.000 mm from the tip of the cylindrical specimen, the next set at 3.007 mm, and so on until reaching 4.316 mm (188 cross-sections at 7 μ m spacing).

The nf data was used to reconstruct a map of crystallographic orientations on an array of square pixels. The forward-simulation-based HEXOMAP reconstruction package [17, 37] was employed for this purpose, achieving high spatial resolution (3 μ m pixel size) and orientation resolution (0.1°). Pixel orientations were optimized based on comparison between forward-simulated and experimental diffraction peaks. The 2D 'slice' reconstructions of each cross-section were then concatenated into a 3D map of crystallographic orientations. The resulting anisotropic voxels (3 μ m × 3 μ m) were made isotropic (3 μ m × 3 μ m) via supersampling without interpolation of the orientations (the supersampling procedure is described in the Supplementary Information). Next, the orientation map was segmented into grains with the PolyProc function package [38], using a misorientation threshold of 0.7° for neighboring voxels. Finally, the mask of the sample boundary was defined with the aid of a conventional, absorption contrast tomography scan [39] collected with the Zeiss Xradia 520 Versa X-ray microscope at the University of Michigan.

In addition to the orientation map, the HEXOMAP algorithm outputs a corresponding map of completeness values [17, 37]; see **Figs. 1(a,b)**. Completeness, C, is defined as the overlap between the experimental and simulated diffraction peaks [35]. By definition, $C \in [0,1]$. It indicates the trustworthiness of the corresponding pixel orientation, where 1 indicates a perfect match between simulated and observed peaks. A review of the HEDM literature shows a lack of consideration for the completeness values of GBs. Instead, attention was given to classifying a region as either recrystallized or deformed [34, 37]. In our case, we do not externally deform the material, and the sample is taken to be fully recrystallized (supported by relatively high grain-averaged completeness values of \sim 0.7). The bulk of large grains exhibit the highest values of C, while the edges of grains show the lowest values of C (where the grain contacts either another grain or the sample surface, *i.e.*, there is a sudden change in orientation or material).

Following reconstruction and grain segmentation, typical post-processing procedures remove low-completeness voxels and small grains that might be attributed to noise [38]. This operation results in a microstructure with false voids in the sample. Frequently, such artifacts are then 'filled in' *via* morphological filters, *e.g.*, image dilation (which can be performed in the software DREAM.3D [24, 40]; see the Supplementary Information for further discussion). While the end-result is a space-filling microstructure, such image processing is nevertheless susceptible to arbitrary selections of numerous parameters (*e.g.*, the shape and size of the morphological

structuring elements). This variability in parameter choices may lead to differences in approaches across similar studies. Another deficiency of the typical post-processing procedure is that image processing does not respect the underlying physics of the microstructure. For example, in **Fig. S1**, we demonstrate an image processing routine performed on a square pixel array that creates and fills a gap between four grains but fails to penalize a quadruple point (unstable in 2D).

To circumvent the above two issues, we introduce a new procedure for post-processing that utilizes a phase-field (PF) model for polycrystalline grain growth. Grains are represented by order parameters η_i that indicate different crystallographic domains ($\eta_i = 1$ within the i^{th} grain and $\eta_i = 0$ elsewhere, with a smooth hyperbolic tangent profile across the interface). The evolution is driven by the reduction of the system free energy,

$$F = \int (f_{bulk} + f_{gradient}) \, dV, \tag{1}$$

where f_{bulk} and $f_{gradient}$ are expressed in terms of the order parameters. The bulk free energy density is given by the form used in [41],

$$f_{bulk} = W \left[\sum_{i=1}^{N} \left(-\frac{1}{2} \eta_i^2 + \frac{1}{4} \eta_i^4 \right) + \frac{3}{2} \sum_{i=1}^{N} \sum_{j>1}^{N} \left(\eta_i^2 \eta_j^2 \right) + \frac{1}{4} \right], \tag{2}$$

where W is the bulk free energy density coefficient that affects the grain boundary thickness, which is a model parameter. The gradient energy term penalizes gradients in the order parameters according to

$$f_{gradient} = \frac{\kappa}{2} \sum_{i=1}^{N} |\nabla \eta_i|^2,$$
(3)

where κ is the gradient energy coefficient. The values for W and κ are related to the grain boundary width l_{gb} according to

$$l_{gb} = 2\sqrt{\frac{2\kappa}{W}}.$$
(4)

Each unique grain in the 2D reconstruction is assigned its own order parameter η_i , which evolves according to the Allen-Cahn equation,

$$\frac{\partial \eta_i}{\partial t} = -M \frac{\delta F}{\delta \eta_i},\tag{5}$$

where M is the PF mobility, which will be further described below, and F is given by Eq. 1. The resulting Eq. 5 was solved numerically using the finite difference method with a uniform spatial mesh and forward Euler time integration with time step size sufficiently small to yield numerical stability ($\Delta t^* = 0.01$). The grid spacing was chosen to be equal to the pixel width in the experiment, $\Delta x = 3 \, \mu m$. When scaling by the average grain radius r_0 , the dimensionless grid spacing is $\Delta x^* = 0.075$, where the superscript * indicates a dimensionless quantity. Since Eq. 5 involves second-order spatial derivatives of the order parameters, it is necessary to adequately resolve the diffuse interfaces to reduce numerical errors of the solution [42, 43]. We chose to use four grid spacings for the grain boundary width, i.e., $l_{qb} = 4\Delta x = 12 \ \mu m$. All parameters used in the PF computations are summarized in **Table 1**. After evolving according to Eq. 5, each pixel (voxel in 3D) was then labeled according to the order parameter with the highest value at that location, and subsequently segmented into specific grain indices to yield the post-processed grain map. The number of the time iterations was determined such that it was sufficient to modify the order parameters in regions with low completeness values. This was accomplished in a separate calculation for which pixels that were below a desired completeness threshold (0.5 in this case) were not assigned to any order parameter; then, Eq. 5 was evolved until the unassigned pixels were filled by neighboring grains (which occurred at approximately $t_f^* = 4.5$). Note that since we are not simulating the physical evolution of the system, time has no physical meaning and therefore no physical units.

Table 1: Dimensional and dimensionless PF parameters.

Parameters	Dimensionless parameters (indicated by *)
W	$W^* = 1$
κ	$ \kappa^* = \frac{\kappa}{Wr_0^2} = \frac{1}{8} \left(\frac{l_{gb}}{r_0}\right)^2 = 0.01125 $
М	$M^* = \frac{M}{M_{max}} = M$

The full proposed workflow is shown in **Fig. 1**. A representative 2D slice of the reconstruction is used to show the orientation and completeness outputs of the HEXOMAP reconstruction algorithm. Instead of creating artificial gaps in the microstructure where the completeness is low, as is the conventional approach [38, 44] we retain all data from the HEXOMAP output and construct the mobility parameter M in the PF evolution equation (Eq. 5) as a function of the completeness C. Specifically, we define M as

$$M = \begin{cases} M_{min} & C > b \\ (M_{max} - M_{min})p(\phi) + M_{min} & a \le C \le b, \\ M_{max} & C < a \end{cases}$$

$$(6)$$

where

$$p(\phi) = \phi^3 (6\phi^2 - 15\phi + 10), \tag{7}$$

$$\phi = \frac{b - C}{b - a}.\tag{8}$$

Here, $p(\phi)$ interpolates between M_{min} and M_{max} in the range $a \le C \le b$. The form of $p(\phi)$ is typically used in PF models of solidification [45] and ensures M is a smooth function. Eq. (6) is plotted in Fig. 2(a). Arrows in Figs. 1(b,c) correspond to line profiles in Fig. 2(b), which show

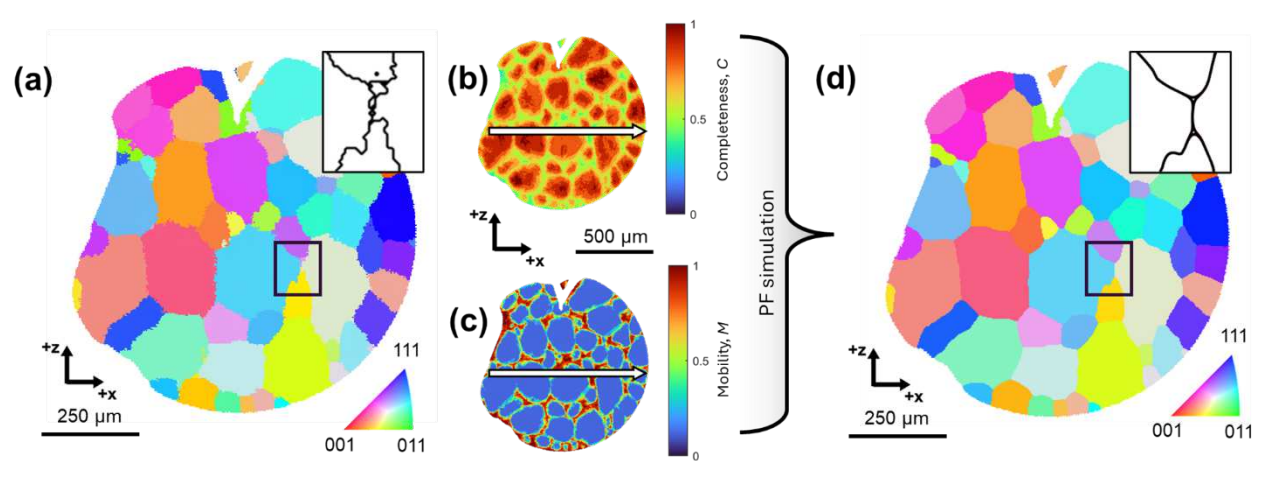


Fig. 1. Data processing workflow starting with HEXOMAP reconstruction outputs of (a) pixel orientations and (b) completeness, from which we calculate the (c) completeness-derived mobility. Finally, (d) gives the output grain map from PF processing, taking segmented grains and (c) as inputs. The insets in (a) and (d) show a magnified view of the same region before and after PF post-processing, within which the black lines represent the GBs.

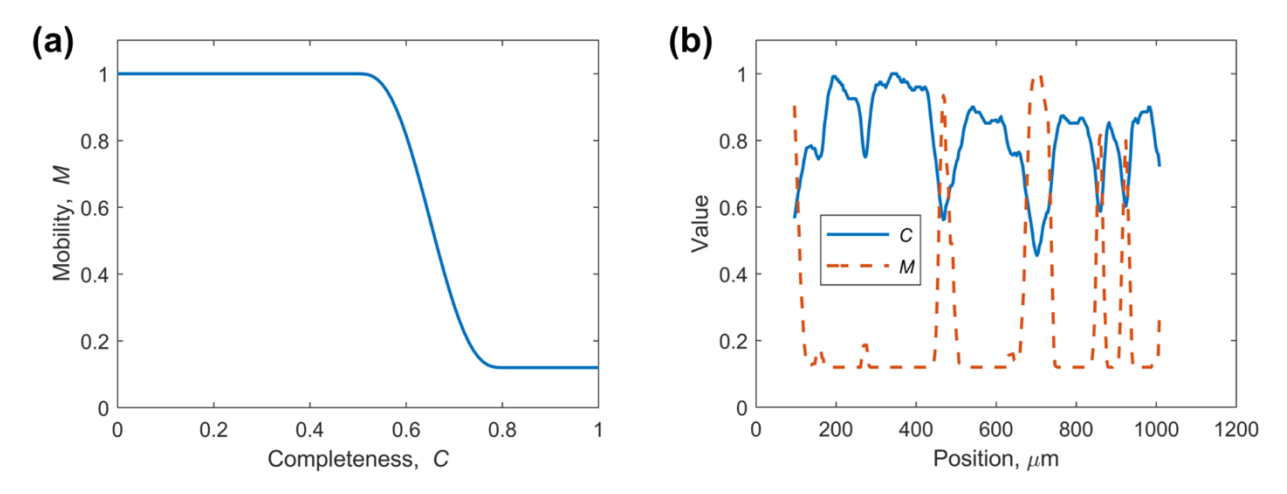


Fig. 2. (a) Plot of relationship between mobility and completeness. (b) Line profiles of completeness, C, and the corresponding mobility, M, versus position, see **Figs. 1(b) and (c)**, respectively. This plot was generated using a centered moving mean that considers five pixels.

the inverse relationship between completeness and mobility. The bounds of the mobility in Eq. (6) are taken from the experimental observations of high and low completeness values. Above the upper completeness limit of b = 0.8 (typical of the bulk), the mobility is highly restricted but nonzero; this has the added advantage that all GBs are mobile enough to achieve a small degree of smoothing. The value for M_{min} (0.12) was set to the ratio of the length scale of the desired smoothing for all grain boundaries (3 pixels) to the length scale of the largest low-completeness region (25 pixels, in 2D). Below the lower completeness limit of a = 0.5(typical of low-completeness grains and TJ points in 2D), the mobility takes on a maximum value, $M_{max} = 1$. The mobility here is unitless because time is not a physical quantity since we are not simulating actual evolution. This helps to 'repair' any higher-order connectivity points by providing sufficient mobility to split them into multiple triple points (see, e.g., the insets of Figs. 1(a,d), which show the evolution of a quadruple point to two triple points separated by a GB). Ultimately, this protocol is intended to preserve the highest-confidence regions of the reconstruction while allowing evolution of the low confidence regions that are most prone to error. While PF models with a constant mobility M have been used previously to reduce the roughness of the GBs [46], the novelty in our approach is that M varies based on the completeness of the reconstruction. The Supplementary Information provides further discussion on the two cases.

We quantified the extent of boundary smoothing in 2D by computing both the circularity of the interior grains and the tortuosity of the individual GBs, before and after PF post-processing. Circularity, c, is defined as $c = 4\pi A/P^2$, where A is the area of a grain and P is the perimeter. This metric has a maximum value of 1 for a circle and approaches 0 for highly irregular or elongated shapes. Grains intersecting the sample surface had an immobile section of their perimeter during PF processing and were not included in this analysis. As a benchmark for

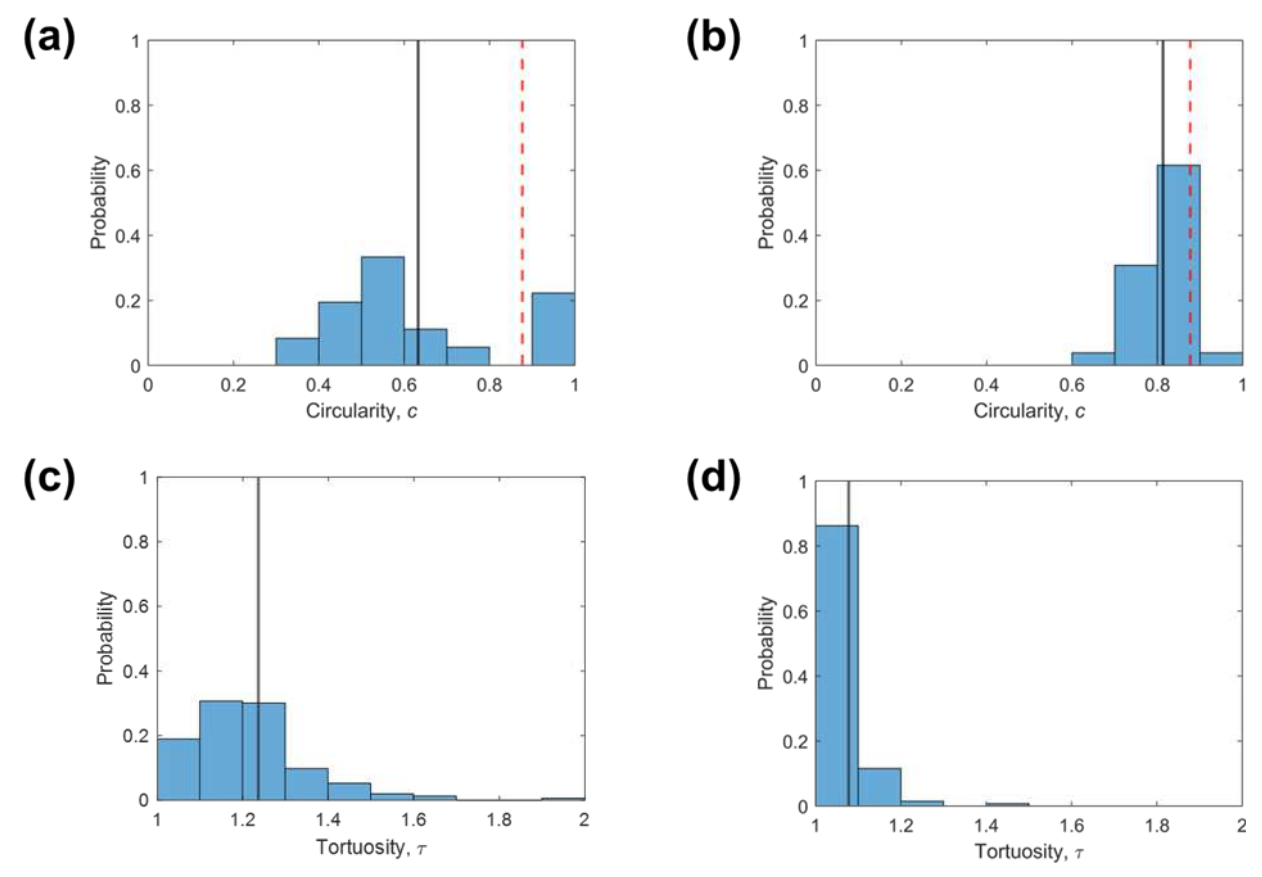


Fig. 1. Evaluation of grain maps, before (left) and after (right) 2D PF processing, according to (a,b) circularity of interior grains and (c,d) tortuosity of grain boundaries. Solid black vertical lines indicate the mean of each distribution. Dashed red vertical lines in (a,b) show mean circularity of normal grains from Ref. [47]. The circularity distribution shifts from 0.63 ± 0.2 to 0.81 ± 0.07 , and tortuosity shifts from 1.23 ± 0.3 to 1.08 ± 0.05 .

comparison, we note that DeCost and Holm [47] found in 2D Monte Carlo Potts simulations that the average circularity of equiaxed grains in a normal grain growth regime is $\bar{c} = 0.877$. **Figs. 3(a,b)** show the distributions in grain circularities. We obtained $\bar{c} = 0.63$ before post-processing and $\bar{c} = 0.81$ after, which is closer to the benchmark value for equiaxed grains. An increase in mean circularity indicates that the grains either became more equiaxed or the GBs became smoother. Since the PF processing runs for a relatively small number of iterations, there should not be major changes in the grain shape (*e.g.* compression), and therefore the change in the circularity can be attributed mainly to the smoothing of the GBs.

The smoothness of the GBs can be separated from the overall shape of the grain by examining the GB tortuosity, τ , which is calculated by identifying the GBs via image processing and computing $\tau = l/l_0$. Here, l is the shortest connected path length (found through the Dijkstra algorithm [48]) between the endpoints of a GB (corresponding to the triple points, in 2D) and l_0 is the Euclidean distance between those same endpoints. In general, tortuosity is large when the

path is winding, smaller for straighter paths, and attains a minimum value of 1 for a perfectly straight path. Unless a GB is faceted [49], it must have $\tau > 1$ owing to its curvature. The calculation of tortuosity is described further in the Supplementary Information. Paths across the entire sample diameter (along multiple, contiguous GBs) were not considered because they would have captured topological information belonging to the arrangement of the grains; here, we sought only to quantify the GB smoothing by the PF post-processing protocol. **Figs. 3(c,d)** shows that the GB tortuosity decreased from 1.23 to 1.08 after PF post-processing. This decrease indicates that the shortest connected path length l was reduced due to smoothing, as also evidenced in the insets of **Figs. 1(a,d)**.

Data processing in 3D is the ultimate goal, as the microstructure captured in any given cross-section is no doubt influenced by its neighboring sections. With this in mind, our protocol can be extended to 3D without loss of generality. We perform PF processing in 3D with the concatenated and supersampled stack of 2D data taken as input (see the Supplementary Information for discussion on the assignment of order parameters). The stopping time in 3D was determined using a separate simulation (analogous to the approach in 2D, described above). The minimum mobility was also determined in analogous fashion; a low-completeness region spanning 40 voxels in 3D yielded the ratio 3:40; thus, $M_{min} = 0.075$. Figs. 4(a,b) show the smoothing of GBs in 3D. For the same 2D slice of the tomographic reconstruction as in Fig. 1(d), Fig. 4(c) shows that 4 additional grains have apparently 'survived' in the 3D PF result, relative to the 2D result. More specifically, after PF processing in 2D, the number of grains decreased from 71 to 60 (15%); the grains that vanish contributed less than 3% of the cross-sectional area. In 3D, grains can not only disappear from but also appear into the plane-of-interest. That is, more degrees of freedom are accessible to the system in higher dimensions [50], hence why 5% more grains (64 in total) remained after PF processing; less than 4% of the voxels

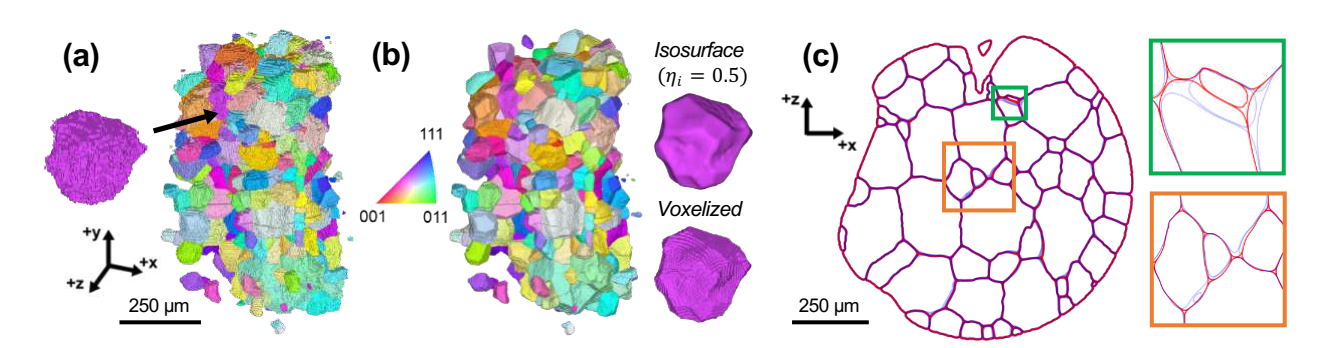


Fig. 4. Proof-of-concept of our approach in 3D. Direct reconstruction (a) before and (b) after PF post-processing, showing only the interior grains of the microstructure in a voxelized representation. Insets show a zoomed-in and isolated view of the grain indicated in (a), and the 'isosurface' inset displays the order parameter representation. (c) 3D results shown for the same slice as in **Fig. 1**, with GBs from 2D and 3D results shown in red and blue, respectively. Boxed regions are magnified for clarity.

were reindexed in due course. Likewise, in the entire 3D volume, less than 4% of voxels were reassigned, and the number of grains decreased from 1161 to 997 (14%).

We performed a quantitative analysis of these 3D results. The 3D analog of circularity is sphericity, S, defined (for the interior grains) as $S = 4\pi r_{eq}^2/\rho^2$, where r_{eq} is the equivalent radius of a grain and ρ is the surface area. This metric has a maximum value of 1 for a sphere and approaches 0 for highly irregular or elongated shapes. Fig. S3 shows distributions of sphericity for the unprocessed data, DREAM.3D-processed data, and the PF processed data (see the Supplementary Information for discussion on the conventional post-processing routine). The mean sphericities are 0.71, 0.72, and 0.86, respectively. For reference, the sphericity of a Kelvin cell is 0.91 [51]. A higher value for the PF processed data than that of the DREAM.3D-processed state implies that the former is more effective at reducing GB surface area via smoothing. Furthermore, we compared our results to that of a 3D front-tracking simulation of grain growth [50]. This work reports an isoperimetric value, I, defined as $I = 36\pi V^2/\rho^3$, where V is the volume of a grain. Whereas sphericity compares the surfaces areas of a grain and a sphere of equivalent volumes, the isoperimetric value compares the volumes of a grain and a sphere of equivalent surface area. Our unprocessed data, DREAM.3D-processed data, and PF-processed data yielded values of 0.38, 0.40, and 0.69, respectively. In comparison, Ref. [50] find I =0.76803 when steady-state is achieved. While such values for circularity and tortuosity are useful as benchmarks, we do not recommend using them as criteria for determining the stopping point in the PF-based approach. The PF processing routine should be generalized enough to be applicable to microstructures with non-equiaxed grains.

In summary, our PF-model-based post-processing protocol offers an alternative to conventional image processing solutions, which may produce or retain non-physical grain configurations. We have demonstrated the utility of our proposed technique by highlighting the splitting of unstable quadruple points (in 2D) into multiple triple points and by quantifying the mesoscale GB roughness using interior grain circularity and GB tortuosity in 2D, and sphericity and the isoperimetric value in 3D. Our study used nf-HEDM data reconstructed by the HEXOMAP algorithm, but this approach can, in principle, be applied to any diffraction-based imaging technique that provides a spatial map of the crystallographic orientations and their associated confidence indices, *e.g.*, EBSD [52] or DCT [12-15]. It can also be extended to polyphase microstructures (such as the dual-phase Cu-Al-Mn shape memory alloy [17, 18, 30, 31]) with artificially rough interfaces; in that case, the interphase boundaries take the place of the GBs here. Finally, the mobility function can be extended to account also for crystallographic effects, such as the grain boundary character, in addition to confidence indices. Broadly, these enhancements will aid efforts in understanding and mapping processing-structure relationships through improved reconstructions of polycrystalline microstructures.

Declaration of Competing Interest

The authors declare that they have no known competing financial interests or personal relationships that could have appeared to influence the work reported in this paper.

Acknowledgements

This work was supported by the National Science Foundation under Award No. DMR-2104786. This research used resources of the Advanced Photon Source, a U.S. Department of Energy (DOE) Office of Science User Facility operated for the DOE Office of Science by Argonne National Laboratory under Contract No. DE-AC02-06CH11357. The computational resources for the HEDM reconstruction were provided by Advanced Research Computing, a division of Information and Technology Services at the University of Michigan, Ann Arbor. The authors would like to thank Robert Suter and He Liu for their guidance in using the HEXOMAP reconstruction package. The computational resources for the PF processing reported in this work were provided by Anvil at the RCAC through allocation No. TG-DMR110007 from the Advanced Cyberinfrastructure Coordination Ecosystem: Services & Support (ACCESS) program, which is supported by National Science Foundation grants #2138259, #2138286, #2138307, #2137603, and #2138296. The authors would like to thank Guanglong Huang and Eymana Maria for their useful discussions about the PF processing.

References

- 1. Smith, C.S., *Grains, phases, and interfaces: An introduction of microstructure.* Trans. Metall. Soc. AIME, 1948. **175**: p. 15-51.
- 2. Gertsman, V. and K. Tangri, *Modelling of intergranular damage propagation*. Acta materialia, 1997. **45**(10): p. 4107-4116.
- 3. Argon, A. and Y. Qiao, *Cleavage cracking resistance of large-angle grain boundaries in Fe-3 wt% Si alloy.* Philosophical Magazine A, 2002. **82**(17-18): p. 3333-3347.
- 4. Lu, N., et al., *Dynamics of Ga penetration in textured Al polycrystal revealed through multimodal three-dimensional analysis.* Acta Materialia, 2021. **217**: p. 117145.
- 5. Palumbo, G., et al., *Grain boundary design and control for intergranular stress-corrosion resistance.* Scripta Metallurgica et Materialia, 1991. **25**(8): p. 1775-1780.
- 6. Shimada, M., et al., Optimization of grain boundary character distribution for intergranular corrosion resistant 304 stainless steel by twin-induced grain boundary engineering. Acta Materialia, 2002. **50**(9): p. 2331-2341.
- 7. Peterson, N., *Diffusion mechanisms and structural effects in grain boundaries*. Journal of Vacuum Science & Technology A: Vacuum, Surfaces, and Films, 1986. **4**(6): p. 3066-3070.
- 8. Kondratev, V. and I.S. Trachtenberg, *Intergranular diffusion in real polycrystals*. physica status solidi (b), 1992. **171**(2): p. 303-315.
- 9. Heidenreich, R. and L. Matheson, *Electron microscopic determination of surface elevations and orientations*. Journal of Applied Physics, 1944. **15**(5): p. 423-435.
- 10. Smith, C.S., *Some elementary principles of polycrystalline microstructure*. Metallurgical Reviews, 1964. **9**(1): p. 1-48.
- 11. Groeber, M.A., et al., *3D reconstruction and characterization of polycrystalline microstructures using a FIB–SEM system.* Materials characterization, 2006. **57**(4-5): p. 259-273.

- 12. Poulsen, H.F., *Three-dimensional X-ray diffraction microscopy: mapping polycrystals and their dynamics*. Vol. 205. 2004: Springer Science & Business Media.
- 13. Jensen, D.J., et al., *X-ray microscopy in four dimensions*. Materials Today, 2006. **9**(1-2): p. 18-25.
- 14. Johnson, G., et al., *X-ray diffraction contrast tomography: a novel technique for three-dimensional grain mapping of polycrystals. II. The combined case.* Journal of Applied Crystallography, 2008. **41**(2): p. 310-318.
- 15. Shahani, A.J., et al., *Characterization of metals in four dimensions*. Materials Research Letters, 2020. **8**(12): p. 462-476.
- 16. Bernier, J.V., et al., *High-energy x-ray diffraction microscopy in materials science*. Annual Review of Materials Research, 2020. **50**: p. 395-436.
- 17. Higgins, M., et al., *Anomalous strain-energy-driven macroscale translation of grains during nonisothermal annealing.* Physical Review Materials, 2021. **5**(7): p. L070401.
- 18. Huang, G., et al., *Phase-Field Modeling of Stored-Energy-Driven Grain Growth with Intra-Granular Variation in Dislocation Density.* Model. Simul. Mat. Sci. Eng., 2024. **accepted**.
- 19. Farver, J.R. and R.A. Yund, *Measurement of oxygen grain boundary diffusion in natural, fine-grained, quartz aggregates.* Geochimica et Cosmochimica Acta, 1991. **55**(6): p. 1597-1607.
- 20. Cecen, A., et al., 3-D microstructure analysis of fuel cell materials: spatial distributions of tortuosity, void size and diffusivity. Journal of The Electrochemical Society, 2012. **159**(3): p. B299.
- 21. Cooper, S.J., et al., *TauFactor: An open-source application for calculating tortuosity factors from tomographic data.* SoftwareX, 2016. **5**: p. 203-210.
- 22. Lee, S., G. Rohrer, and A. Rollett, *Three-dimensional digital approximations of grain boundary networks in polycrystals*. Modelling and Simulation in Materials Science and Engineering, 2014. **22**(2): p. 025017.
- 23. Ratanaphan, S., Y. Yoon, and G.S. Rohrer, *The five parameter grain boundary character distribution of polycrystalline silicon.* Journal of materials science, 2014. **49**: p. 4938-4945.
- 24. Kelly, M.N., et al., *The five parameter grain boundary character distribution of α-Ti determined from three-dimensional orientation data*. Acta Materialia, 2016. **111**: p. 22-30.
- 25. Kammer, D. and P. Voorhees, *The morphological evolution of dendritic microstructures during coarsening*. Acta materialia, 2006. **54**(6): p. 1549-1558.
- 26. Patterson, B.R., et al., *Affinities for topological arrangements in grain structures*. Acta materialia, 2014. **79**: p. 411-420.
- Watanabe, T., *Grain boundary engineering: historical perspective and future prospects.* Journal of materials science, 2011. **46**(12): p. 4095-4115.
- 28. Sun, T., et al., *Surface and grain-boundary scattering in nanometric Cu films.* Physical Review B, 2010. **81**(15): p. 155454.
- 29. Kim, C.-S., A.D. Rollett, and G.S. Rohrer, *Grain boundary planes: New dimensions in the grain boundary character distribution.* Scripta materialia, 2006. **54**(6): p. 1005-1009.
- 30. Omori, T., et al., *Abnormal grain growth induced by cyclic heat treatment*. Science, 2013. **341**(6153): p. 1500-1502.
- 31. Kusama, T., et al., *Ultra-large single crystals by abnormal grain growth.* Nature communications, 2017. **8**(1): p. 354.
- 32. Suter, R., et al., Forward modeling method for microstructure reconstruction using x-ray diffraction microscopy: Single-crystal verification. Review of scientific instruments, 2006. 77(12).
- 33. Hefferan, C., et al., *Tests of microstructure reconstruction by forward modeling of high energy X-ray diffraction microscopy data.* Powder Diffraction, 2010. **25**(2): p. 132-137.
- 34. Li, S., et al., *Three-dimensional plastic response in polycrystalline copper via near-field high-energy X-ray diffraction microscopy*. Journal of Applied Crystallography, 2012. **45**(6): p. 1098-1108.

- 35. Li, S. and R. Suter, *Adaptive reconstruction method for three-dimensional orientation imaging.* Journal of Applied Crystallography, 2013. **46**(2): p. 512-524.
- 36. Lin, B., et al., *Observation of annealing twin nucleation at triple lines in nickel during grain growth.* Acta Materialia, 2015. **99**: p. 63-68.
- 37. Liu, H., et al. 3D in-situ stop action study of recrystallization in additively manufactured 316L stainless steel: reconstruction optimization and observations. in IOP Conference Series: Materials Science and Engineering. 2022. IOP Publishing.
- 38. Kang, J., et al., *PolyProc: a modular processing pipeline for X-ray diffraction tomography*. Integrating Materials and Manufacturing Innovation, 2019. **8**: p. 388-399.
- 39. Hounsfield, G.N., *Computerized transverse axial scanning (tomography): Part 1. Description of system.* The British journal of radiology, 1973. **46**(552): p. 1016-1022.
- 40. Groeber, M.A. and M.A. Jackson, *DREAM. 3D: a digital representation environment for the analysis of microstructure in 3D.* Integrating materials and manufacturing innovation, 2014. **3**(1): p. 56-72.
- 41. Moelans, N., B. Blanpain, and P. Wollants, *Quantitative analysis of grain boundary properties in a generalized phase field model for grain growth in anisotropic systems.* Physical Review B, 2008. **78**(2): p. 024113.
- 42. Eiken, J. *Numerical solution of the phase-field equation with minimized discretization error.* in *IOP Conference Series: Materials Science and Engineering.* 2012. IOP Publishing.
- 43. Eggleston, J.J., *Phase -field models for thin film growth and Ostwald ripening*. 2001, Northwestern University: United States -- Illinois. p. 138.
- 44. Renversade, L., et al., Comparison between diffraction contrast tomography and high-energy diffraction microscopy on a slightly deformed aluminium alloy. IUCrJ, 2016. **3**(1): p. 32-42.
- 45. Boettinger, W.J., et al., *Phase-field simulation of solidification*. Annual review of materials research, 2002. **32**(1): p. 163-194.
- 46. Petrich, L., et al., Efficient fitting of 3D tessellations to curved polycrystalline grain boundaries. Frontiers in Materials, 2021. 8: p. 760602.
- 47. DeCost, B.L. and E.A. Holm, *Phenomenology of abnormal grain growth in systems with nonuniform grain boundary mobility*. Metallurgical and Materials Transactions A, 2017. **48**: p. 2771-2780.
- 48. Dijkstra, E.W., *A note on two problems in connexion with graphs*. Numerische Mathematik, 1959. **1**(1): p. 269-271.
- 49. Straumal, B., et al., *grain boundary faceting–roughening phenomena*. Journal of materials science, 2016. **51**: p. 382-404.
- 50. Mason, J.K., et al., *Geometric and topological properties of the canonical grain-growth microstructure*. Physical Review E, 2015. **92**(6): p. 063308.
- 51. Princen, H. and P. Levinson, *The surface area of Kelvin's minimal tetrakaidecahedron: The ideal foam cell (?)*. Journal of colloid and interface science, 1987. **120**(1): p. 172-175.
- 52. Wilkinson, A.J. and T.B. Britton, *Strains, planes, and EBSD in materials science*. Materials today, 2012. **15**(9): p. 366-376.

Supplementary Information

Order parameter assignment for 3D phase-field code

For 2D evolution, each cross-section of the experimental sample contains roughly 100 grains, so it is feasible to assign each grain its own order parameter. However, for the 3D microstructure (which contains over 1000 grains), this was no longer possible due to the large memory requirement. To make the 3D PF processing computationally tractable, each order parameter tracked multiple grains.

In order to prevent grain coalescence during evolution between two grains sharing the same order parameter, grains were assigned to order parameters ensuring that they were sufficiently spaced using an exclusion zone. This was accomplished by the following algorithm in MATLAB:

- 1. For each unique grain index i in the 3D grain orientation map, generate a binary field n_i where $n_i = 1$ at voxels equal to i and $n_i = 0$ elsewhere;
- 2. For each binary field, generate a distance field d_i from the grain surface using the built-in MATLAB bwdist() function;
- 3. Set the voxels of the binary fields n_i to 1 if the value of their corresponding distance field d_i is less than or equal the exclusion distance d_{ex} ;
- 4. Loop over every pair of binary fields n_i and n_j to check if they overlap, i.e., $n_i(r) = n_j(r) = 1$, and construct an $N \times N$ adjacency matrix;
- 5. Input the adjacency matrix into a greedy coloring algorithm to obtain k sets of indices m corresponding to grains that are sufficiently spaced;

The k sets of grain indices are used to generate k order parameters η_i which are initialized to 1 at the locations of grain indices within the set.

Conventional processing routine

We first demonstrate the conventional post-processing routine in an illustration, and then we apply it to the actual HEDM data. In general, the conventional routine involves applying size and completeness thresholds to mask out grains or voxels that are deemed untrustworthy [38]. These artificial voids are filled in (or inpainted) with image dilation in software such as DREAM.3D [24, 40]. Image dilation may result in the formation of unstable higher-connectivity configurations, such as a QN in 2D, demonstrated in **Fig. S1**. Our PF method uses a more informed approach – one that adheres to the physics of capillary-driven microstructure evolution, thus avoiding thermodynamically unstable configurations.

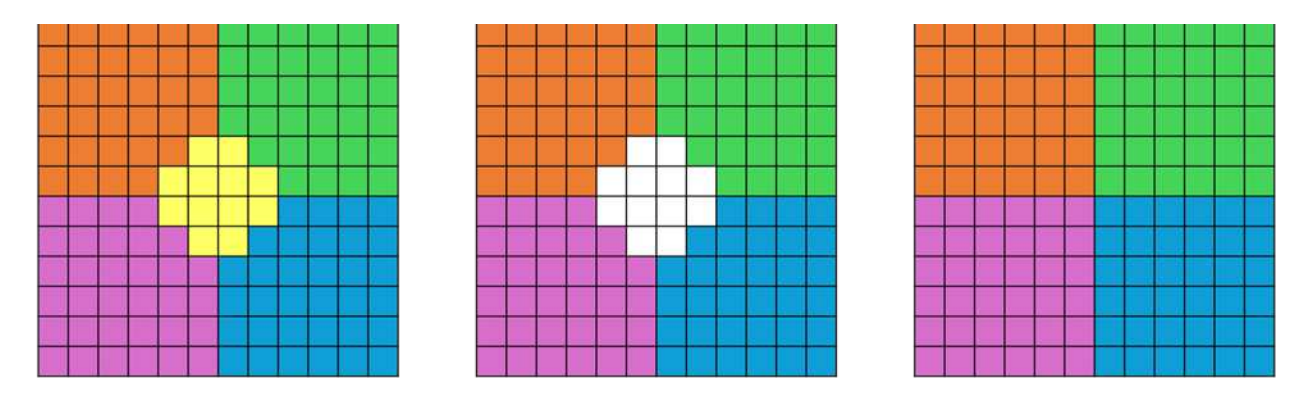


Fig. S1. Schematic of an image post-processing routine. (a) Reconstruction of 5 grains (colored). (b) Middle yellow grain is removed due to either size or completeness filtering and leaves a false void (white). (c) Image dilation fills the false void but creates an unstable 2D quadruple node.

In **Fig. S2** below, we present in (a-d) a conventional 3D workflow and (e) the result of our 3D phase-field processing, for comparison. A cross-section of the 3D reconstruction in (a) is depicted in (b-e). We apply size and completeness thresholds to unassign voxels to grains. Some of those voxels (but not all) adorn the grain boundaries and triple junctions since they possess low completeness (in practice, one could unassign *all* grain boundary voxels by examining their local neighborhoods). The size threshold is 19 voxels (where each voxel measures $3 \times 3 \times 3 \ \mu m^3$), corresponding to a volume of 8 voxels in the native HEDM resolution (where each voxel is $3 \times 7 \times 3 \ \mu m^3$). The completeness threshold is 0.5. Voxels are unindexed based on these thresholds, and then the surrounding grains are dilated into the unindexed regions. The result of this conventional processing routine contains grain boundaries with a residual roughness, as will be quantified below.

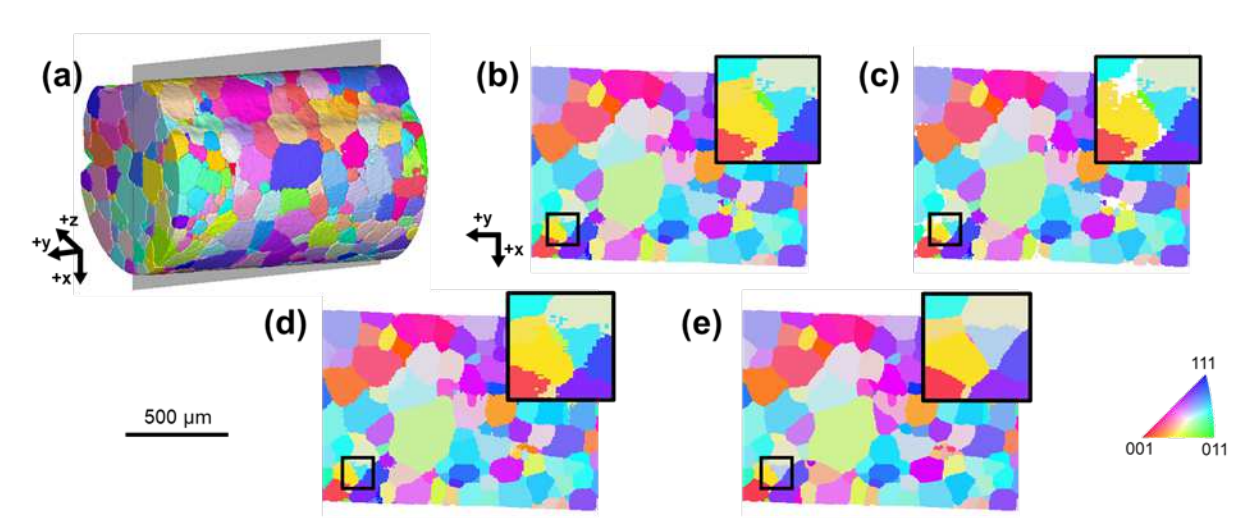


Fig. S2. (a-d) Demonstration of conventional processing pipeline. (a) 3D view of the HEXOMAP reconstruction. (b-e) 2D slices corresponding to the gray plane cut through the volume in (a). Application of (b) a size threshold of 8 voxels in the native HEDM resolution, followed by (c) a completeness threshold of 0.5, and finally (d) dilation using 'Fill Bad Data' in DREAM.3D [40]. (e) After 3D PF processing.

In **Fig. S3**, we present a quantitative comparison of the degree of grain boundary smoothing achieved through the conventional image processing and proposed PF processing routines. The sphericity of interior grains was calculated for the size-thresholded data, the phase-field-processed data, and the DREAM.3D-processed data. The size-thresholded data is used to avoid including many negligibly small, equiaxed grains that artificially raise the sphericity to 1. The distributions of sphericity for each dataset are shown in **Fig. S3**. The means of each distribution can be compared to the sphericity of a low-surface-area tetrakaidecahedron, the Kelvin cell [51].

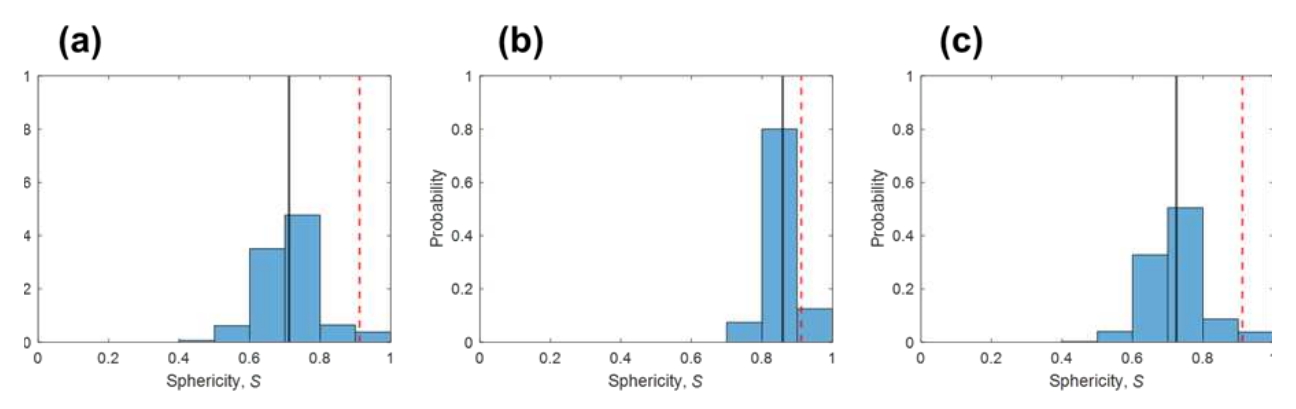


Fig. S3. Evaluation of grain maps (a) before, (b) after phase-field processing, and (c) after dilation using DREAM.3D, following the same routine indicated in Fig. S2. Solid black vertical lines indicate the means of each distribution. Dashed red vertical lines give the sphericity of a Kelvin cell, 0.91, from Ref. [51]. The distribution shifts from 0.71 \pm 0.08 to 0.86 \pm 0.04 for the phase-field processing. The DREAM.3D processing yields a distribution with 0.72 \pm 0.08.

Supersampling from native HEDM resolution to isotropic voxels

Due to the 3- μ m reconstructed pixel size (in the *x*-*z* plane) and the 7- μ m layer spacing (along *y*), the HEDM data is naturally anisotropic. We elected to perform a supersampling procedure in the *y* direction to arrive at isotropic pixels; see **Fig. S4** for a schematic illustration.

This operation was performed before the grain segmentation step, meaning the operating array contained voxel-wise orientation information. Although it is tempting to interpolate orientations for the newly created slices, we recommend against it because it may join grains that otherwise do not satisfy the voxel-to-voxel misorientation criterion of 0.7° used in the grain segmentation procedure. For example, two grains with a misorientation of 1.2° between 2 layers of HEDM data would be combined, because interpolation would provide a path of voxels that connects them via two 0.6° misorientations over the same distance. The non-integer ratio of 7:3, combined with the decision not to interpolate, means that one in every three layers is overrepresented, and the other two layers are underrepresented. To avoid this, in future work, it is recommended to set the desired pixel size as a divisor of the inter-layer spacing, e.g., 3.5 µm.

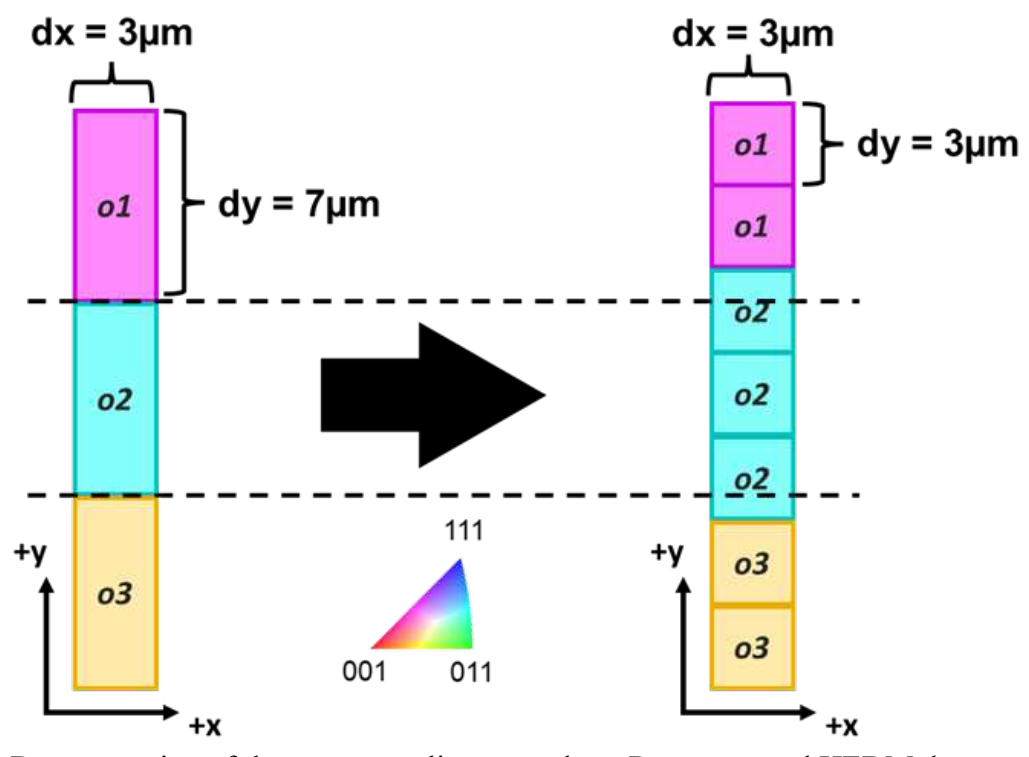


Fig. S4. Demonstration of the supersampling procedure. Reconstructed HEDM data are inherently anisotropic (left), which we correct for *via* supersampling (right). Orientations (colored) are not interpolated because doing so would disrupt the downstream grain segmentation (possibly joining grains with a small misorientation). The non-integer ratio of 7:3 results in an overrepresentation of the orientation *o2*.

Specification of image processing required for calculation of tortuosity

The quantification of the grain boundary tortuosity, τ , begins with the pixelated representation of our data (in 2D), such that it is possible to make a comparison to the original HEXOMAP reconstruction. First, we must identify the pixels belonging to the grain boundary. The pixels are taken to be any pixels on the perimeter of grain i that lie adjacent to any pixel on the perimeter of grain j. The tortuosity is then computed by finding the shortest connected path along grain boundary pixels. For any pair of pixels, there is a Dijkstra shortest path [48] between them. The longest path among that set of "shortest paths" (l) is associated with the two endpoints that define the beginning and end of the grain boundary. These endpoints are saved and the Euclidean distance between them (l_0) is also determined. Finally, the tortuosity τ is computed as $\tau = l/l_0$. Fig. S5 gives a proof-of-concept of this procedure for the unprocessed and PF-processed data.

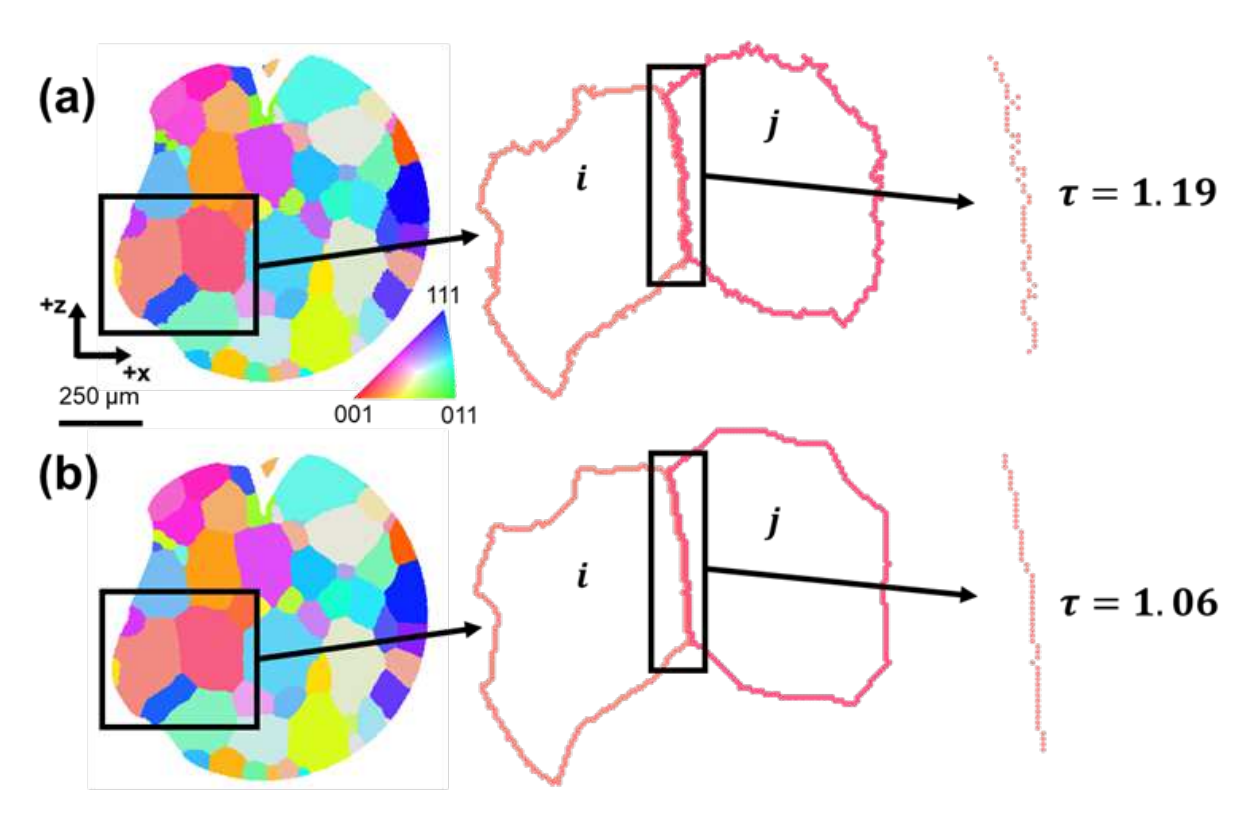


Fig. S5. Demonstration of image processing for the calculation of tortuosity τ . In 2D, a grain boundary between grains i and j is defined by those pixels on the perimeter of i (j) that have a nearest-neighbor pixel in j (i). Tortuosity is then computed on the graph of the identified grain boundary pixels. This approach is shown for (a) the unprocessed and (b) PF-processed data. The tortuosity of the same grain boundary reduces by over 10%, consistent with Figs. 3(c-d).

Comparison between constant and completeness-based mobility

We compare PF processing with constant mobility (M=1) and completeness-based mobility at $t_f^*=4.5$ in Fig. S6. Regions of significant difference are shown inset. It is clear that in the case of constant mobility, small grains undergo significantly more evolution, either rapidly shrinking or disappearing as a result of capillarity-driven evolution. In the case of completeness-based mobility, small grains with high-completeness are more resistant to shrinkage, despite their size. The difference in the two cases would become even more pronounced if PF processing runs for longer times t_f^* .

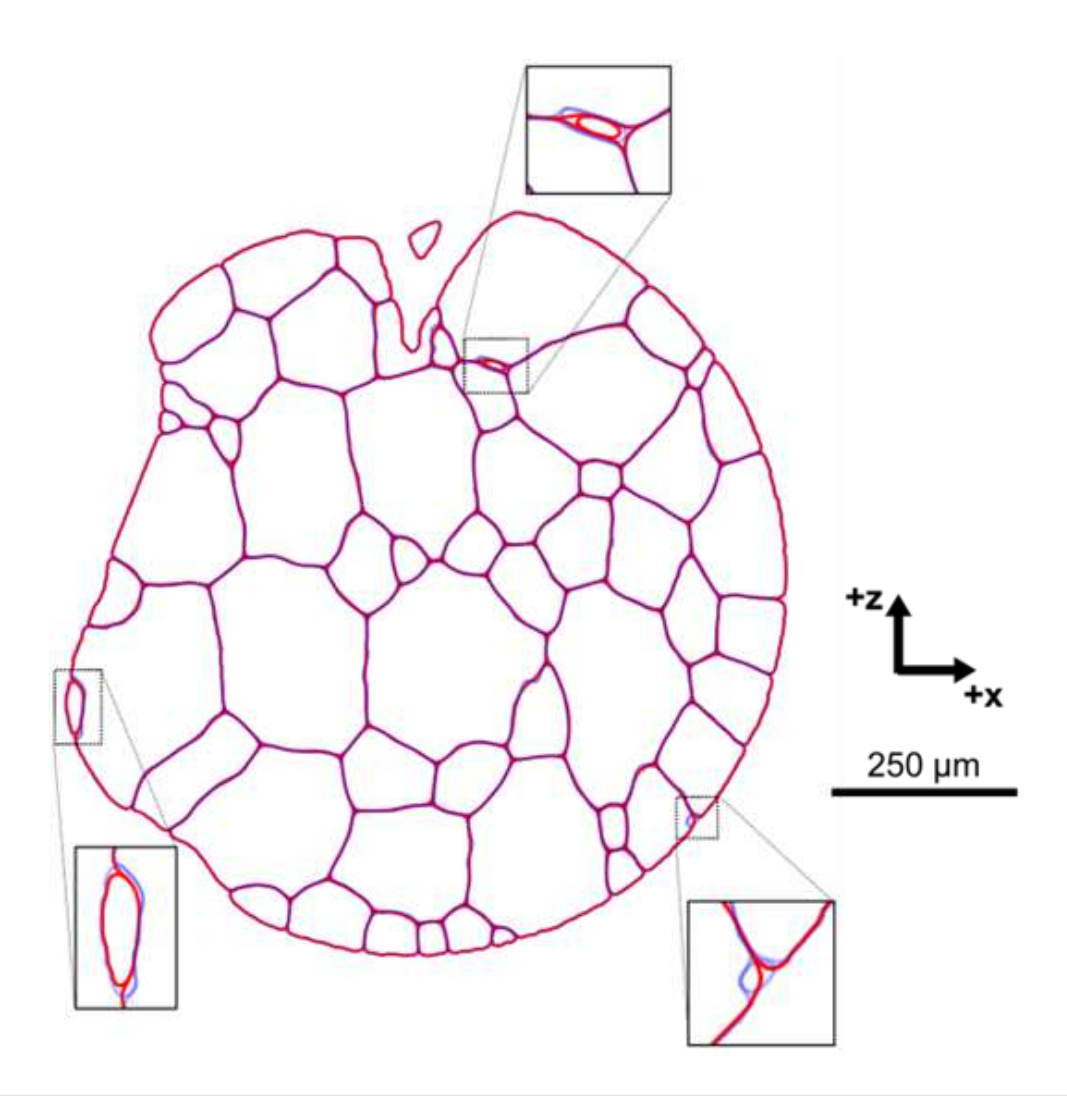


Fig. S6. Overlay of PF processed reconstruction with constant mobility (red contours) and completeness-based mobility (black contours). Insets show zoomed-in regions that illustrate differences in the two cases, for clarity.